Time-Optimal Path Planning in Uncertain Flow Fields Using Stochastic Dynamically Orthogonal Level Set Equations

by

Quantum Jichi Wei

Submitted to the Department of Mechanical Engineering
in partial fulfillment of the requirements for the degree of

Bachelor of Science in Mechanical Engineering

at the

MASSACHUSETTS INSTITUTE OF TECHNOLOGY

June 2015

Signature redacted

Author .....
Department of Mechanical Engineering
May 22, 2015

Signature redacted

Certified by .....
Pierre F.J. Lermusiaux
Associate Professor
Thesis Supervisor

Signature redacted

Accepted by .....
Anette Hosoi
Professor of Mechanical Engineering
Undergraduate Officer

Time-Optimal Path Planning in Uncertain Flow Fields Using Stochastic Dynamically Orthogonal Level Set Equations

by

Quantum Jichi Wei

Submitted to the Department of Mechanical Engineering
on May 22, 2015, in partial fulfillment of the
requirements for the degree of
Bachelor of Science in Mechanical Engineering

Abstract

Path-planning has many applications, ranging from self-driving cars to flying drones, and to our daily commute to work. Path-planning for autonomous underwater vehicles presents an interesting problem: the ocean flow is dynamic and unsteady. Additionally, we may not have perfect knowledge of the ocean flow. Our goal is to develop a rigorous and computationally efficient methodology to perform path-planning in uncertain flow fields. We obtain new stochastic Dynamically Orthogonal (DO) Level Set equations to account for uncertainty in the flow field. We first review existing path-planning work: time-optimal path planning using the level set method, and energy-optimal path planning using stochastic DO level set equations. We build on these methods by treating the velocity field as a stochastic variable and deriving new stochastic DO level set equations. We use the new DO equations to simulate a simple canonical flow, the stochastic highway. We verify that our results are correct by comparing to corresponding Monte Carlo results. We explore novel methods of visualizing the results of the equations. Finally we apply our methodology to an idealized ocean simulation using Double-Gyre flows.

Thesis Supervisor: Pierre F.J. Lermusiaux
Title: Associate Professor

Acknowledgments

Thanks to:

- Pierre, for advising me on this thesis and much more
- Deepak, for his guidance and great explanations
- Everyone in the MSEAS group, for welcoming me
- My brothers of Chi Phi at MIT, who are always there for me
- My teammates on the lacrosse team, for being so much fun
- Anyone else I have been lucky enough to meet while at MIT

- My family, without whom I would not be here

Contents

1 Introduction **15**

1.1 Background and Motivation 15

1.2 Past Work 17

2 Methodology **19**

2.1 Theory 19

2.1.1 DO expansion notation 19

2.1.2 Einstein Summation Notation 19

2.1.3 Level-Set Methods 20

2.1.4 Problem Statement 21

2.1.5 DO-MC Gamma Level Set Equations 22

2.1.6 Derivation of DO-MC Gamma Level Set Equations 23

2.1.7 Conclusions 26

2.2 Numerical Methods 26

2.2.1 3d Matrix Manipulation 26

3 Applications **31**

3.1 Canonical Flow - Stochastic Highway 31

3.1.1 Verification of DO run 33

3.1.2 Reachability Front vs Highway Speed 34

3.1.3 2d Histogram of Reachability Fronts 35

3.2 Stochastic Double-Gyre Flow 39

3.2.1 Comparison of DO and MC level set 41

3.2.2 Reachability Front vs Time to Reach 41
3.2.3 2d histogram of Reachability Fronts 42
3.3 Conclusions 47

4 Future Work **49**
4.1 KL and Taylor Gamma 49
4.2 Further Analysis of Current Results 49
4.3 Energy-Optimal Path Planning 50

5 Conclusions **51**

List of Figures

1-1 In path-planning, the goal is to get from point A to point B while optimizing a certain quantity. This can include time, safety, energy, or data collected. In ocean flows, the flow field varies with time and space. Flow field strength can be the same order of magnitude as vehicle speed. (Lolla et al., 2012) 16

2-1 A vehicle starts at point y_s in a flow field $V(x,t)$. At time t, the region R indicates all points that the vehicle can reach. ∂R indicates the reachability front at time t. (Lolla et al., 2014) 21

2-2 The dimensions of the some coefficient equation matrices are shown. g is the total number of grid cells, s is the number of DO modes, r is number of flow field modes, and MC is the number of MC realizations. 27

2-3 Matrix reshaping and multiplication is shown. Care must be taken during both operations so that the proper quantities are multiplied with each other. The product is a matrix of dimensions $[g, MC]$, to match the other terms in the coefficient equation. 29

3-1 The stochastic highway lies in the blue region. Within this region, the flow is steady with respect to time and space. The strength of the flow is a stochastic variable. Outside of highway, the flow field is zero. . . 32

3-2 (a) We compare the Times to Reach obtained by DO and MC runs. A perfect match between DO and MC runs would appear as a line with a slope of 1. One can see qualitatively that the results are fairly accurate. (b) We quantify the error in Time to Reach by taking the difference between MC and DO runs. In this example, $dt = 0.25$. The maximum error here is two time steps, and 97% of realizations have less than 0.5% error. 33

3-3 We compare a single realization's zero level set for the DO and MC simulations of the stochastic highway. The curves are nearly identical. Fréchet distance is normalized by grid cell size. The maximum Fréchet distance is less than the spacial resolution of the simulation. 34

3-4 We plot the reachability fronts of every single realization. Each reachability front is colored according to its realization's highway strength (0.5 to 1.5 colorbar). Portions of the reachability front that have not yet entered the stochastic highway are unaffected. Portions that have seen uncertainty begin to develop a stochastic DO level-set band. The stochastic DO level-set band flips over on itself, splitting the domain into two regions. The highway flow helps us reach points in one region, and prevents us from reaching points in the other. 36

3-5 2d histogram of the zero level sets of all realizations. The total number of DO realizations is 2,000. We truncate the color axis to verify that we have correctly counted the level sets. 37

3-6 2d histogram of the zero level sets of all realizations. The total number of DO realizations is 2,000. The reachability fronts are very dense when the stochastic DO level-set band is narrow, and become sparser when the stochastic DO level-set band widens. 38

3-7 The wind-driven double gyre flow varies is dynamic, varying with time and space. The figure shows snapshots of the velocity flow field at various non-dimensional times during the simulation. 40

3-8 We compare a single realization's zero level set for the DO and MC simulations of the double gyre flow. The curves are nearly identical. Fréchet distance is normalized by grid cell size. The maximum Fréchet distance is less than the spacial resolution of the simulation. 41

3-9 We plot the zero level sets of every single realization, colored by Time to Reach. Regions with a very wide stochastic DO level-set band indicate large amounts of uncertainty compared to regions with a narrow stochastic DO level-set band. The stochastic DO level-set band flips several times due to the complexity of the flow. 42

3-10 2d histogram of the zero level sets with an alternate coloring scheme. The total number of DO realizations is still 5,000. We truncate the color axis to verify that we have correctly counted the zero level sets. All grid cells with a value of 0 appear blue. All grid cells with a finite value appear purple. This plot should look very similar to Figure 3-9. 43

3-11 We create a 2d histogram of the zero level sets to visualize the probability distribution function. The total number of DO realizations is 5,000. The reachability fronts are not uniformly distributed. The faint outlines indicate that the fronts tend to gather at the extremes of the stochastic DO level-set band. 44

3-12 2d histogram of the zero level sets with an alternate coloring scheme. The total number of DO realizations is still 5,000. The regions of blue that lie within the purple indicate regions within the stochastic DO level-set band that are very sparse. 45

3-13 Plot of 100 random zero level sets. Realizations are less likely to have zero level sets towards the middle of the stochastic DO level-set band. Zero level sets are more likely to appear at the extremes of the band. 46

List of Tables

3.1 Parameters used for DO and MC simulations of the stochastic highway flow 32
3.2 Parameters used for DO simulations of the double-gyre flow 39

Chapter 1

Introduction

1.1 Background and Motivation

Suppose we want to get to school and are standing at the bus stop in the morning. We can use a smartphone app to check when the bus will arrive. If it is going to arrive very soon, it might make sense to wait for the bus. We will get to school faster and expend less energy compared to walking all the way. However if the bus is delayed, it may actually end up being faster to walk to school. With the help of the smartphone app, we have some good information about the options available to us, and can make a decision so that we make it to school on time.

This decision making process is an example of path-planning. We participate in path planning all the time. We may be driving somewhere and avoid taking the freeway because there is bad traffic. We decide to walk across the Harvard Bridge rather than take the bus because of rush hour. Or perhaps it is rush hour and we decide to take the bus anyways because it is raining outside. We may not think much of it, but path-planning is a powerful ability. In this work, we focus on the problem of giving robots or autonomous vehicles the ability to make these decision.

In path planning, a vehicle navigates from point A to point B while optimizing a certain quantity, as shown in Figure 1-1. In time-optimal path planning, the objective is to get from point A to point B in the least amount of time (Lolla, 2012). Or one might want to choose a path such that the usefulness of data collected along the

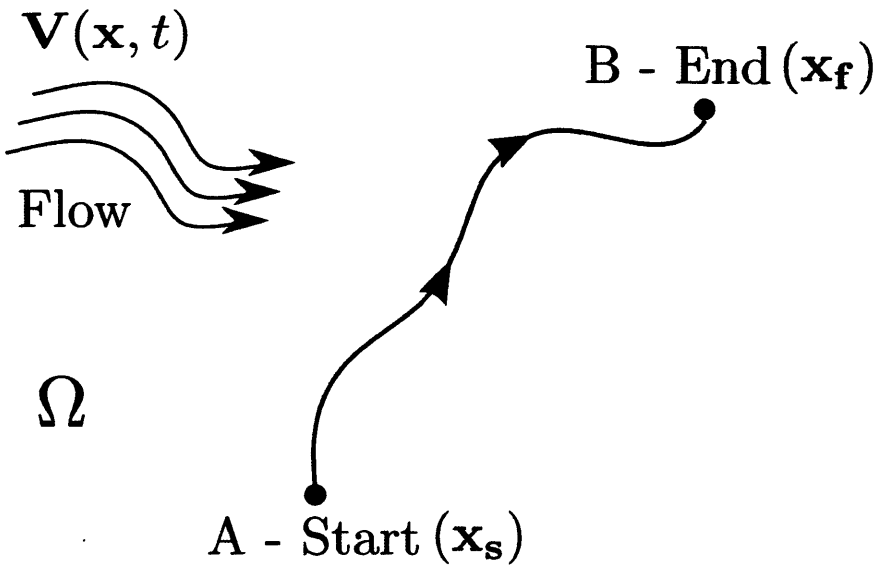

Figure 1-1: In path-planning, the goal is to get from point A to point B while optimizing a certain quantity. This can include time, safety, energy, or data collected. In ocean flows, the flow field varies with time and space. Flow field strength can be the same order of magnitude as vehicle speed. (Lolla et al., 2012)

route is maximized (Lermusiaux, 2007). In energy optimal path planning, we seek to minimize the amount of energy consumed along the route (Subramani, 2014).

Automated underwater vehicles (AUVs) and underwater gliders have a multitude of applications - including ocean floor mapping, search and rescue, oil and gas exploration, and ocean monitoring, among others. In order to make the most use out of these vehicles, it is necessary to develop efficient path-planning methods to guide these vehicles.

Standard path planning algorithms may not be suitable for ocean applications. Many of the these methods work well for static environments, such as on land in fixed surrounding conditions. However, ocean flows are significant and dynamic. Standard methods of path planning may be too computationally expensive or too inaccurate for vehicles to use navigate on-the-fly. The development of time-optimal path planning by Lolla et al. (2012) has proven to be an efficient, rigorous method of navigating through a strong and dynamic ocean flow. These level set methods have also been adapted to energy optimal path planning (Subramani, 2014).

Ocean flows also present interesting possibilities. Suppose there is a "highway flow" between you and your destination. If the highway is flowing towards your target, you can take advantage of the highway and ride it towards your destination. The highway can help you get to your destination in less time and spending less energy. However, if the highway is working against you, you may want to spend as little time as possible in the highway or even avoid it altogether.

This thesis focuses on time-optimal path planning in uncertain flow fields. We extend the dynamically orthogonal (DO) level set equations developed for energy-optimal path planning to account for uncertainties in the flow field (Subramani, 2014, and Subramani et al., 2015). These uncertainties often arise from ocean forecasts or limited ocean data. We implement these new level set equations and verify their results for canonical flows against Monte Carlo simulation. We also present the results of a stochastic DO level-set simulation on a stochastic double gyre flow. Finally, we also begin to explore methods of visualizing the results of the new level set equations.

The path planning methods discussed here can be extended well beyond the ocean. Quadcopters are quite versatile due to their easy of maneuverability: Amazon has proposed using these vehicles as a method of delivering packages. Google and Facebook have proposed methods of providing internet access by using fleets of balloons and drones, respectively. In all of these applications, a chief concern is energy usage and optimum time.

1.2 Past Work

Path-planning has been studied in depth. However, less work has been done on path-planning in a dynamic and unsteady flow field, for example in ocean currents (Lolla et al. 2014).

Lolla et al. (2014) developed a method of using level sets to achieve time-optimal path planning in an ocean. In the level sets method, the zero level set is defined as the "reachability front" of the vehicle (Osher and Sethian, 1988). The region that lies within this front corresponds to all the points that a vehicle could reach within

a time t. This "reachability front" is evolved according to rigorous partial differential equations (PDEs) until it intersects with the target point. Then backtracking is used to determine the path the vehicle should take to reach its destination in the shortest amount of time.

Subramani (2014) builds on this approach to achieve energy-optimal path planning. However, the vehicle speed is treated as a random variable. This results in a stochastic partial differential equation. Stochastic PDEs can be extremely computationally expensive to solve, which is not conducive to on-the-fly path planning.

The dynamically orthogonal (DO) field equations by Sapsis and Lermusaiux (2009) provides an efficient way to solve such stochastic PDEs. The authors start with a stochastic PDE which describes a continuous dynamic stochastic field. They take advantage of non-linearities in the flow. The DO condition is imposed: "the rate-of-change of the stochastic subspace is dynamically orthogonal to the subspace itself (Ueckermann et al. 2013)". Therefore, DO modes and stochastic coefficients only evolve according to the dynamics of the system. This cuts down significantly on the computational cost needed to solve the relevant stochastic PDEs.

Subramani (2014) derived new stochastic DO level set equations to achieve energy-optimal path planning. This thesis build on that work to account for uncertainty in the flow field.

Chapter 2

Methodology

In this chapter we go over the theory and notations used to obtain and describe the new DO level set equations that we developed and employ.

2.1 Theory

2.1.1 DO expansion notation

We use the shorthand DO notation as described by Subramini (2014) to describe stochastic quantities. If $\bullet$ is a stochastic variable, then it can be decomposed into the following components:

$$\bullet = \bar{\bullet} + A_i \tilde{\bullet}_i \tag{2.1}$$

where $\bar{\bullet}$ is the mean of $\bullet$. $\tilde{\bullet}_i$ and A_i are the modes and corresponding stochastic coefficients of $\bullet$, respectively.

2.1.2 Einstein Summation Notation

Einstein summation notation is a method of briefly indicating summation over indexed terms. Suppose the level set ϕ has three modes. We can express the components of ϕ as follows:

$$\phi = \sum_{i=1}^{3} Y_i \tilde{\phi}_i = Y_1 \tilde{\phi}_1 + Y_2 \tilde{\phi}_2 + Y_3 \tilde{\phi}_3 \tag{2.2}$$

This is rather cumbersome, especially if we decide to add more modes. Therefore, we employ the Einstein notation. With this notation, if we see the same index twice within the same term, then we sum the terms over all values of the index.

$$\phi = Y_i \tilde{\phi}_i \tag{2.3}$$

2.1.3 Level-Set Methods

A level set of a function is the set of all points that are equal to a constant value. Lolla (2012) pioneered a new methodology of using level sets to track the *reachability front* of a vehicle in a dynamic flow field. Suppose a vehicle is traveling through a flow field $v(x,t)$ with engine speed F, as in Figure 2-1. The equation that governs the evolution of the reachability front is as follows:

$$\frac{\partial \phi}{\partial t} + F|\nabla \phi| + v \cdot \nabla \phi = 0 \tag{2.4}$$

$\phi(x,t)$ represents the viscosity solution of the level set equations. At time t, all points that lie within and on the zero level set contour ($\phi < 0$) represent all points that the vehicle can reach at time t.

The reachability front evolves normal to itself at a rate proportional to the engine speed. If there is no underlying flow field, then the level sets will be circular.

Suppose there is no flow field. The reachability front is therefore dictated only by the maximum vehicle speed. Each successive level curve is a larger circle, with the radius corresponding to the maximum vehicle speed multiplied by the time elapsed.

However, if there is a flow field, then the vehicle is being advected in addition to motion due to its own propulsion. The level curves can become distorted. The flow may push the vehicle in one direction, and work against the vehicle from going in another direction.

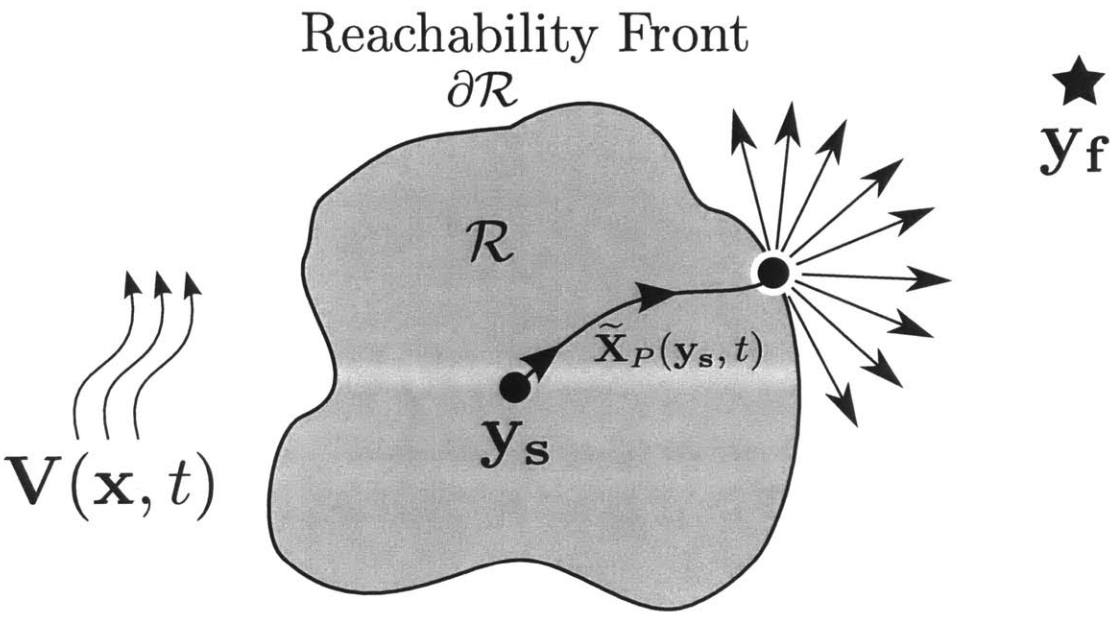

Figure 2-1: A vehicle starts at point y_s in a flow field $V(x,t)$. At time t, the region R indicates all points that the vehicle can reach. ∂R indicates the reachability front at time t. (Lolla et al., 2014)

If there is an underlying flow field, then the level sets are advected by the flow. Even if the vehicle speed is zero, the reachability front will still expand.

2.1.4 Problem Statement

Suppose a vehicle is traveling through the ocean. We consider the vehicle speed, F, and ocean flow, v, to be stochastic variables:

$$F = \bar{F} + z\tilde{F} \tag{2.5}$$

$$v = \bar{v} + \beta_j \tilde{v}_j \tag{2.6}$$

We also consider the level set variable ϕ to be stochastic.

$$\phi = \bar{\phi} + Y_i \tilde{\phi}_i \tag{2.7}$$

The stochastic level set equations are as follows:

$$\frac{\partial \phi}{\partial t} = -F|\nabla \phi| - v \cdot \nabla \phi \tag{2.8}$$

For brevity, we define a new variable γ:

$$\gamma = |\nabla \phi| \tag{2.9}$$

We now rewrite the stochastic level set equations using a DO expansion and substituting for γ:

$$\frac{\partial \bar{\phi}}{\partial t} + Y_i \frac{\partial \tilde{\phi}_i}{\partial t} + \tilde{\phi}_i \frac{dY_i}{dt} = -(\bar{F} + z\tilde{F})\gamma - (\bar{v} + \beta_j \tilde{v}_j) \cdot \nabla(\bar{\phi} + Y_i \tilde{\phi}_i) \tag{2.10}$$

2.1.5 DO-MC Gamma Level Set Equations

We compute γ with a Monte-Carlo simulation rather than utilizing a DO approach. We forgo the possibility of increased efficiency, but the resulting equations are more simple. The mean, coefficient, and mode equations are shown below.

The derivation assumes that Y_i and β_j are centered stochastic variables, i.e. $E[Y_i] = E[\beta_j] = 0$. Teh result of this derivation is:

$$\frac{\partial \bar{\phi}}{\partial t} = -\left[\bar{F}\mathrm{E}[\gamma] + \tilde{\mathrm{F}}\mathrm{E}[\mathrm{z}\gamma] + \bar{\mathrm{v}} \cdot \nabla \bar{\phi} + \mathrm{C}_{\beta_j \mathrm{Y_i}} \tilde{\mathrm{v}}_\mathrm{j} \cdot \nabla \tilde{\phi}_\mathrm{i}\right] \tag{2.11}$$

$$\frac{dY_i}{dt} = -\Big\langle \bar{F}(\gamma - E[\gamma]) + \tilde{F}(z\gamma - E[z\gamma]) + \tilde{v}_j \cdot \nabla \tilde{\phi}_k (\beta_j Y_k - C_{\beta_j Y_k}) + Y_k \bar{v} \cdot \nabla \tilde{\phi}_k + \beta_j \tilde{v}_j \cdot \nabla \bar{\phi}, \tilde{\phi}_i \Big\rangle \tag{2.12}$$

$$\frac{\partial \tilde{\phi}}{\partial t} = Q_i - \left\langle Q_i, \tilde{\phi}_n \right\rangle \tilde{\phi}_n \tag{2.13}$$

where $Q_i = -C^{-1}_{Y_j Y_i}\left[\bar{F}E[Y_j\gamma] + \tilde{F}E[zY_j\gamma] + C_{Y_j\beta_k}\tilde{v}_k \cdot \nabla\bar{\phi} + E[Y_j\beta_k Y_i]\tilde{v}_k \cdot \nabla\tilde{\phi}_i\right] - \bar{v} \cdot \nabla\tilde{\phi}_i$

We thus obtained two stochastic partial differential equations (Equations 2.11 and 2.13) and one stochastic differential equation (Equation 2.12). A derivation of the equations is provided in the next section.

2.1.6 Derivation of DO-MC Gamma Level Set Equations

In this section, we outline the steps needed to derive the new DO level set equations with flow uncertainty.

$$\frac{\partial \bar{\phi}}{\partial t} + Y_i \frac{\partial \tilde{\phi}_i}{\partial t} + \tilde{\phi}_i \frac{dY_i}{dt} = -(\bar{F} + z\tilde{F})\gamma - (\bar{v} + \beta_j \tilde{v}_j) \cdot \nabla(\bar{\phi} + Y_i \tilde{\phi}_i) \tag{2.14}$$

To obtain the mean equation, we take the expectation of both sides of the equation. We assume that $E[Y_i] = E[\beta_j] = 0$.

$$\mathrm{E}\left[\frac{\partial \bar{\phi}}{\partial t} + \cancel{Y_i \frac{\partial \tilde{\phi}_i}{\partial t}} + \cancel{\tilde{\phi}_i \frac{dY_i}{dt}}\right] = -\mathrm{E}\Big[\bar{F}\gamma + z\tilde{F}\gamma + \bar{v} \cdot \nabla\bar{\phi} + \cancel{\beta_j \tilde{v}_j \cdot \nabla\bar{\phi}} + \cancel{Y_i \bar{v} \cdot \nabla\tilde{\phi}_i} + \beta_j Y_i \tilde{v}_j \cdot \nabla\tilde{\phi}_i\Big] \tag{2.15}$$

The mean equation follows:

$$\frac{\partial \bar{\phi}}{\partial t} = -\left[\bar{F}\mathrm{E}[\gamma] + \tilde{\mathrm{F}}\mathrm{E}[\mathrm{z}\gamma] + \bar{\mathrm{v}} \cdot \nabla\bar{\phi} + \mathrm{C}_{\beta_j \mathrm{Y_i}} \tilde{\mathrm{v}}_\mathrm{j} \cdot \nabla\tilde{\phi}_\mathrm{i}\right] \tag{2.16}$$

Next, we move on to derive the coefficient equation. We take the inner product of Equation 2.14 with respect to the modes of the level set.

$$\left\langle \frac{\partial \bar{\phi}}{\partial t}, \tilde{\phi}_n \right\rangle + Y_i \left\langle \frac{\partial \tilde{\phi}_i}{\partial t}, \tilde{\phi}_n \right\rangle + \frac{dY_i}{dt} \left\langle \tilde{\phi}_i, \tilde{\phi}_n \right\rangle = \left\langle (\bar{F} + z\tilde{F})\gamma + \bar{v} \cdot \nabla\bar{\phi} + \beta_j \tilde{v}_i \cdot \nabla\bar{\phi} + Y_i \bar{v} \cdot \nabla\tilde{\phi}_i + \beta_j Y_i \tilde{v}_j \cdot \nabla\tilde{\phi}_i, \tilde{\phi}_n \right\rangle \tag{2.17}$$

We seek the coefficient equation, i.e. we want to isolate the $\frac{dY_i}{dt}$ term. First, we apply the Dynamically Orthogonal condition:

$$\left\langle \frac{\partial \tilde{\phi}_i}{\partial t}, \tilde{\phi}_n \right\rangle = 0 \tag{2.18}$$

Next, to obtain the first term on the left hand side of Equation 2.17, we take the

inner product of the mean equation with respect to the modes of the level set:

$$\left\langle \frac{\partial \bar{\phi}}{\partial t}, \tilde{\phi}_n \right\rangle = -\left\langle \bar{F}E[\gamma] + \bar{F}E[z\gamma] + \bar{v} \cdot \nabla \bar{\phi} + C_{\beta_j Y_i} \tilde{v}_j \cdot \nabla \tilde{\phi}_i, \tilde{\phi}_n \right\rangle \tag{2.19}$$

Now we can substitute Equation 2.19 into Equation 2.17:

$$\frac{dY_i}{dt}\left\langle \tilde{\phi}_i, \tilde{\phi}_n \right\rangle = -\Big\langle \bar{F}(\gamma - E[\gamma]) + \tilde{F}(z\gamma - E[z\gamma]) + \tilde{v}_j \cdot \nabla \tilde{\phi}_i(\beta_j Y_i - C_{\beta_j Y_i}) + Y_i \bar{v} \cdot \nabla \tilde{\phi}_i + \beta_j \tilde{v}_j \cdot \nabla \bar{\phi}, \tilde{\phi}_n \Big\rangle \tag{2.20}$$

Due to the orthogonality of modes:

$$\left\langle \tilde{\phi}_i, \tilde{\phi}_n \right\rangle = \begin{cases} 1, & \text{if } i = n. \\ 0, & \text{otherwise.} \end{cases} \tag{2.21}$$

Therefore, only one term in the summation on the left hand side of equation 2.20 stays alive. This leads us to our final coefficient equation. Note the change in indices.

$$\frac{dY_i}{dt} = -\Big\langle \bar{F}(\gamma - E[\gamma]) + \tilde{F}(z\gamma - E[z\gamma]) + \tilde{v}_j \cdot \nabla \tilde{\phi}_k(\beta_j Y_k - C_{\beta_j Y_k}) + Y_k \bar{v} \cdot \nabla \tilde{\phi}_k + \beta_j \tilde{v}_j \cdot \nabla \bar{\phi}, \tilde{\phi}_i \Big\rangle \tag{2.22}$$

Finally, we need to find the mode equation. We multiply Equation 2.14 by the coefficients of the level set, Y_i, and then take the expectation of both sides:

$$E\left[\cancel{Y_j \frac{\partial \bar{\phi}}{\partial t}} + Y_j Y_i \frac{\partial \tilde{\phi}_i}{\partial t} + Y_j \frac{dY_i}{dt} \tilde{\phi}_i\right] = -E\Big[Y_j \gamma(\bar{F} + z\tilde{F}) + \cancel{Y_j \bar{v} \cdot \nabla \bar{\phi}} + Y_j \beta_k \tilde{v}_k \cdot \nabla \bar{\phi} + Y_j Y_i \bar{v} \cdot \nabla \tilde{\phi}_i + Y_j \beta_k Y_i \tilde{v}_k \cdot \nabla \tilde{\phi}_i\Big] \tag{2.23}$$

$$C_{Y_jY_i}\frac{\partial\tilde{\phi}_i}{\partial t}+C_{Y_j\frac{dY_i}{dt}}\tilde{\phi}_i=-\Big[\bar{F}E[Y_j\gamma]+\tilde{F}E[zY_j\gamma+C_{Y_j\beta_k}\tilde{v}_k\cdot\nabla\bar{\phi}$$
$$+C_{Y_jY_i}\bar{v}\cdot\nabla\tilde{\phi}_i+E[Y_j\beta_kY_i]\tilde{\phi}_i\cdot\nabla\tilde{\phi}_i\Big] \quad (2.24)$$

Remember that we want to find the mode equation. Let us isolate the $C_{Y_j\frac{dY_i}{dt}}$ term. We multiply equation 2.29 by the coefficients of the level set, Y_i, and take the expectation of both sides.

$$E[Y_j\frac{dY_i}{dt}]=-E\Big\langle\bar{F}(Y_j\gamma-\cancel{Y_jE[\gamma]}+\tilde{F}(Y_jz\gamma-\cancel{Y_jE[z\gamma]})+(Y_j\beta_jY_k-\cancel{Y_jC_{\beta_jY_k}})\tilde{v}_1\cdot\nabla\tilde{\phi}_k$$
$$+Y_jY_k\bar{v}\cdot\nabla\tilde{\phi}_k+Y_j\beta_k\tilde{v}_1\cdot\nabla\bar{\phi},\tilde{\phi}_i\Big\rangle \quad (2.25)$$

This yields:

$$C_{Y_j\frac{dY_i}{dt}}=-\Big\langle\bar{F}E[Y_j\gamma]+\tilde{F}E[Y_jz\gamma]+E[Y_j\beta_jY_k]\tilde{v}_1\cdot\nabla\tilde{\phi}_k$$
$$+C_{Y_jY_k}\bar{v}\cdot\nabla\tilde{\phi}_k+C_{Y_j\beta_k}\tilde{v}_1\cdot\nabla\bar{\phi},\tilde{\phi}_i\Big\rangle \quad (2.26)$$

We can now plug this in to Equation 2.24 and multiply the appropriate terms by the inverse of the covariance, $C^{-}_{Y_jY_i}1$ to find the modes equation.

$$\frac{\partial\tilde{\phi}}{\partial t}=-\Big[C^{-1}_{Y_jY_i}[\bar{F}E[Y_j\gamma]+\tilde{F}E[zY_j\gamma]+C_{Y_j\beta_k}\tilde{v}_k\cdot\nabla\bar{\phi}+E[Y_j\beta_kY_i]\tilde{v}_k\cdot\nabla\tilde{\phi}_i]+\bar{v}\cdot\nabla\tilde{\phi}_i\Big]$$
$$+\Big\langle C^{-1}_{Y_jY_i}[\bar{F}E[Y_j\gamma]+\tilde{F}E[zY_j\gamma]+C_{Y_j\beta_k}\tilde{v}_k\cdot\nabla\bar{\phi}+E[Y_j\beta_kY_i]\tilde{v}_k\cdot\nabla\tilde{\phi}_i]+\bar{v}\cdot\nabla\tilde{\phi}_i\Big],\tilde{\phi}_n\Big\rangle\tilde{\phi}_n \quad (2.27)$$

We can rewrite the mode equation as follows:

$$\frac{\partial \tilde{\phi}}{\partial t} = Q_i - \left\langle Q_i, \tilde{\phi}_n \right\rangle \tilde{\phi}_n$$

where $Q_i = -C^{-1}_{Y_j Y_i} \left[\bar{F} E[Y_j \gamma] + \tilde{F} E[z Y_j \gamma] + C_{Y_j \beta_k} \tilde{v}_k \cdot \nabla \bar{\phi} + E[Y_j \beta_k Y_i] \tilde{v}_k \cdot \nabla \tilde{\phi}_i \right] - \bar{v} \cdot \nabla \tilde{\phi}_i$

2.1.7 Conclusions

We derived the new DO level set equations for uncertain flow fields. We utilize stochastic representations of the vehicle speed, ocean flow, and level sets. A MC approach was used to evaluate γ as opposed to a DO approach. A DO approach would likely be more efficient, but the MC approach is sufficient for the first foray into working with uncertain flow fields. We hope to build on this work by deriving the appropriate level set equations for both KL and Taylor representation of γ, similar to Subramani et al. (2015).

2.2 Numerical Methods

Implementation of the DO level set equations builds on code written by members of the MIT MSEAS group. The DO level set equations for uncertain flow fields are very similar to the DO level set equations for certain flow fields. Therefore we have modified the Energy-Optimal Path Planning code to work with uncertain flow fields. The majority of the code is written in MATLAB; the rest is C++.

2.2.1 3d Matrix Manipulation

The addition of flow field uncertainty introduces a new level of complexity to the DO level set equations: 3d matrices. The mean, coefficient, and mode equations all contain terms which we construct as 3d matrices. We reproduce the level set equations below, with the relevant terms underlined.

$$\frac{\partial \bar{\phi}}{\partial t} = - \left[\bar{F} \mathrm{E}[\gamma] + \tilde{\mathrm{F}} \mathrm{E}[z\gamma] + \bar{\mathrm{v}} \cdot \nabla \bar{\phi} + \underline{\mathrm{C}_{\beta_j \mathrm{Y}_i} \tilde{\mathrm{v}}_j \cdot \nabla \tilde{\phi}_i} \right] \tag{2.28}$$

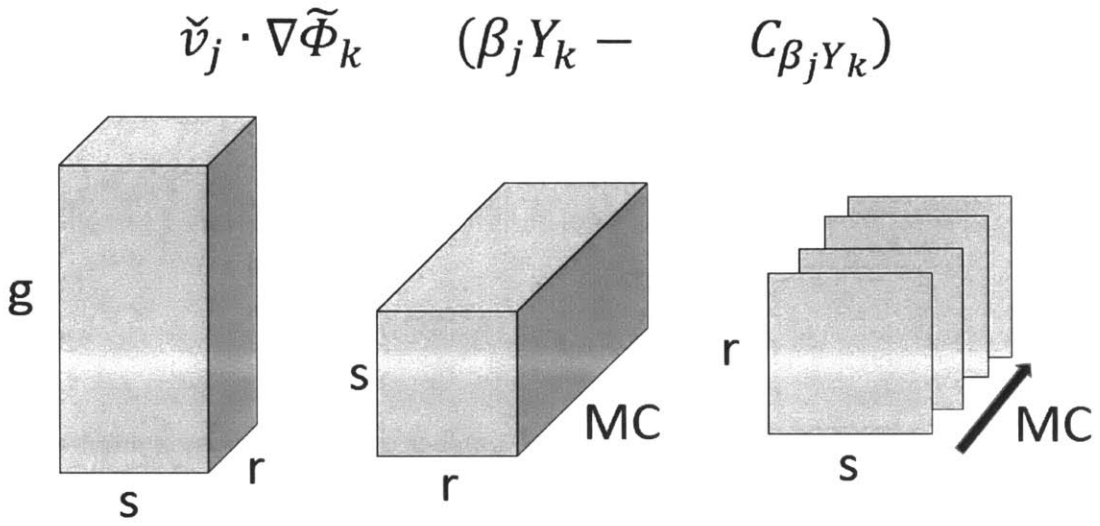

Figure 2-2: The dimensions of the some coefficient equation matrices are shown. g is the total number of grid cells, s is the number of DO modes, r is number of flow field modes, and MC is the number of MC realizations.

$$\frac{dY_i}{dt} = -\Big\langle \bar{F}(\gamma - E[\gamma]) + \tilde{F}(z\gamma - E[z\gamma]) + \underline{\tilde{v}_j \cdot \nabla\tilde{\phi}_k(\beta_j Y_k - C_{\beta_j Y_k})} + Y_k \bar{v} \cdot \nabla\tilde{\phi}_k + \beta_j \tilde{v}_j \cdot \nabla\bar{\phi}, \tilde{\phi}_i \Big\rangle \quad (2.29)$$

$$\frac{\partial\tilde{\phi}}{\partial t} = Q_i - \left\langle Q_i, \tilde{\phi}_n \right\rangle \tilde{\phi}_n$$
$$\text{where } Q_i = -C^{-1}_{Y_j Y_i}\left[\bar{F}E[Y_j\gamma] + \tilde{F}E[zY_j\gamma] + C_{Y_j\beta_k}\tilde{v}_k \cdot \nabla\bar{\phi} + \underline{E[Y_j\beta_k Y_i]\tilde{v}_k \cdot \nabla\tilde{\phi}_i}\right] - \bar{v} \cdot \nabla\tilde{\phi}_i \quad (2.30)$$

We handle these new terms as 3d matrices for increased efficiency of computation. In order to produce sensible results, we need to carefully construct the 3d matrices so that the correct quantities are multiplied with each other. In order to integrate these results with the rest of the equations, the 3d matrices must then be properly reshaped into 2d matrices.

We will illustrate the process of constructing and reshaping the 3d matrices needed to solve the coefficient equation. The approach is similar to that needed for the mode equation. The mean equation is even more simple.

We present the dimensions of the three relevant coefficient equation matrices below. The dimensions of the matrices are also illustrated above in Figure 2-2.

$$\dim(\tilde{v}_j \cdot \nabla\tilde{\phi}_k) = [g, s, r] \tag{2.31}$$

$$\dim(\beta_j Y_k) = [s, r, MC] \tag{2.32}$$

$$\dim(C_{\beta_j Y_k}) = [r, s] \tag{2.33}$$

g is the total number of grid cells, s is the number of DO modes, r is number of flow field modes, and MC is the number of MC realizations. We require identical dimensions for matrix addition, so we transpose and repeat $C_{\beta_j Y_k}$ so that it matches the dimensions of $\beta_j Y_k$.

In order to integrate these terms with the rest of the coefficient equation, we need to end up with a 2d matrix. We reshape the matrices properly and then carefully multiply them so that the proper terms are multiplied with each other. We reshape $\tilde{v}_j \cdot \nabla\tilde{\phi}_k$ to a matrix of dimensions $[g, sr]$. The sum of matrices is reshaped to dimensions $[sr, MC]$. The product of these matrices gives us a matrix of dimension $[g, MC]$ to match the other terms in the coefficient equation. We illustrate the process in Figure 2-3.

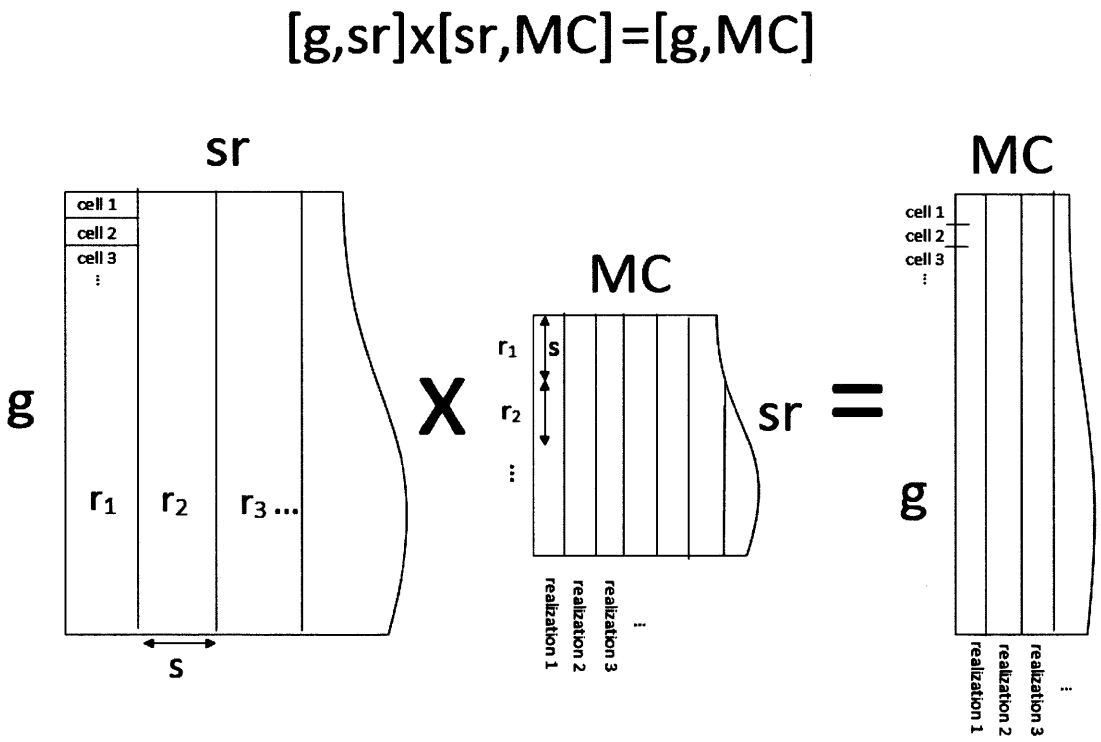

Figure 2-3: Matrix reshaping and multiplication is shown. Care must be taken during both operations so that the proper quantities are multiplied with each other. The product is a matrix of dimensions $[g, MC]$, to match the other terms in the coefficient equation.

Chapter 3

Applications

All simulations were run with constant vehicle speed, although the code can support F as a stochastic variable. Future work should look into variable F, with a focus on effective methods of analyzing and visualizing the results.

3.1 Canonical Flow - Stochastic Highway

We start by investigating a canonical flow, i.e. the stochastic highway flow. The highway flow is not necessarily representative of a real-life ocean flow. However, the results of a DO simulation of the highway flow can be verified against results of a corresponding MC simulation. Once the DO simulation has been verified, we can be more confident that it will produce accurate results for more complex and realistic flows.

The highway lies in the region $0.4 < y < 0.6$. Within the highway, the flow field is steady with respect to time and space. However, the strength of the flow is a stochastic variable. Everywhere outside of the highway region, the flow field is zero.

We consider the time-optimal path planning problem. Our vehicle starts at the point $(0.2, 0.2)$ with the target point at $(0.8, 0.8)$. We ran both a DO and MC simulation for this set-up with 2,000 realizations.

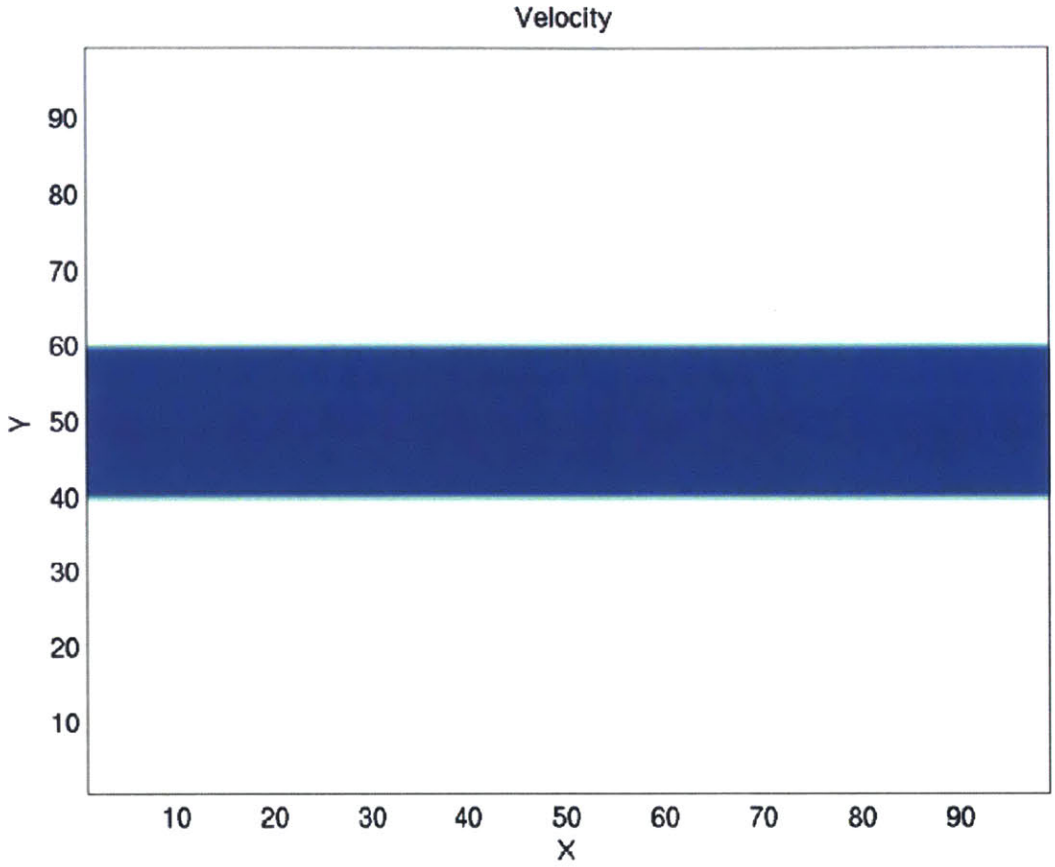

Figure 3-1: The stochastic highway lies in the blue region. Within this region, the flow is steady with respect to time and space. The strength of the flow is a stochastic variable. Outside of highway, the flow field is zero.

Parameter	Value	Description
a	100	Size of domain in x-direction
b	100	Size of domain in y-direction
N_x	100	Number of cells in x-direction
N_y	100	Number of cells in y-direction
dx	1	Spatial discretization in x-direction
dy	1	Spatial discretization in y-direction
T	100	Total time of simulation
dt	0.25	Time Step
s	100	Number of DO modes
r	1	Number of flow field modes
m	2,000	Number of DO and MC samples

Table 3.1: Parameters used for DO and MC simulations of the stochastic highway flow

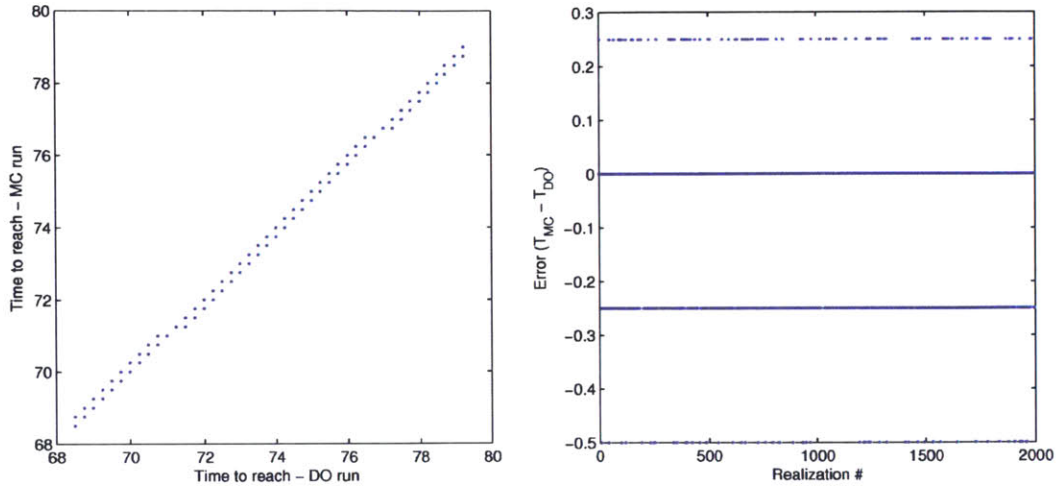

(a) (b)

Figure 3-2: (a) We compare the Times to Reach obtained by DO and MC runs. A perfect match between DO and MC runs would appear as a line with a slope of 1. One can see qualitatively that the results are fairly accurate. (b) We quantify the error in Time to Reach by taking the difference between MC and DO runs. In this example, $dt = 0.25$. The maximum error here is two time steps, and 97% of realizations have less than 0.5% error.

3.1.1 Verification of DO run

We verify the results by comparing the Time to Reach the target for each realization (Figure 3-2(a)). The times obtained by the DO run are nearly identical to the corresponding times from the MC run: the maximum error is two time steps, and 97% of realizations have less than 0.5% error.

The results from the MC run match the DO run. This confirms that the DO level set equations are correct.

The comparison of Times to Reach indicates that the DO runs are accurate. We further verify the DO results by graphing the zero level set (reachability front) of one sample from both the DO and MC runs (Figure 3-3). Qualitatively, the zero level sets appear to be nearly identical. We can quantify the difference between these two curves by calculating the discrete Fréchet distance (Alt and Godau, 1995, and Subramani, 2014).

The Fréchet distance is a measure of how similar (or dissimilar) two curves are.

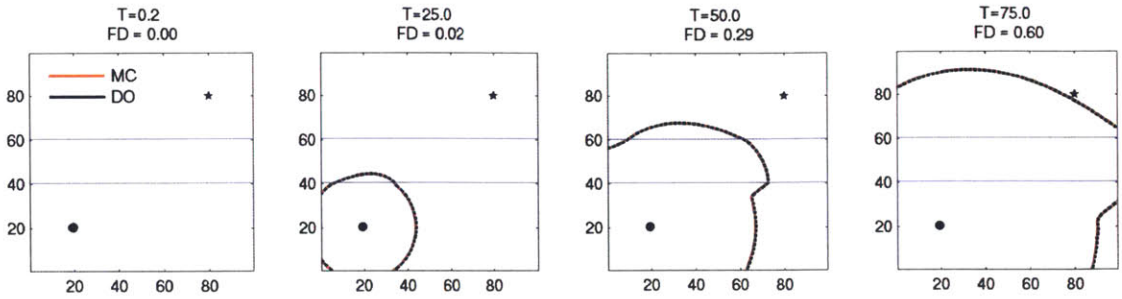

Figure 3-3: We compare a single realization's zero level set for the DO and MC simulations of the stochastic highway. The curves are nearly identical. Fréchet distance is normalized by grid cell size. The maximum Fréchet distance is less than the spacial resolution of the simulation.

Suppose a dog and an owner walk on separate paths from one endpoint to the other, without backtracking. The Fréchet distance is the minimum length of the leash needed to connect the dog to its owner along this route.

Here, we normalize the Fréchet Distance by the size of the grid cells. The maximum Fréchet Distance between the DO and MC zero level sets (FD=0.60) is on the same order of magnitude as our grid cells.

3.1.2 Reachability Front vs Highway Speed

Now we look at how the uncertain highway speed affects the reachability front. For this analysis, we use the DO results exclusively. At each time step, we plot the zero levels for each of our realizations, as shown in Figure 3-4. In this example, there are 2,000 realizations and therefore 2,000 zero level sets. Each zero level set is colored differently based on the strength of that realization's highway. Highway strength is normalized by U_{ref}, a reference velocity.

At early time steps, before the realizations reach the stochastic highway, all of the zero level set curves are the same. This makes sense. Until we hit the stochastic highway, our results should all be the same as a deterministic simulation with a single flow field velocity (here zero) and given a unique vehicle speed.

Once the realizations reach the stochastic highway, the zero level set curves begin to evolve differently. A *stochastic DO level-set band* begins to develop. The width

of the band spans the distance between the "fastest" and "slowest" realizations. The stochastic DO level-set band grows wider with each time step, as uncertainty propagates. However, the band does not develop uniformly. We see that the stochastic DO level-set band is widest within the stochastic highway, the region with the most uncertainty.

At some point in the domain, the stochastic DO level-set band narrows and then flips over. This inflection point divides the reachability fronts into two different regimes. The highway helps us reach all points on the right side of the inflection point. The stronger the highway, the faster we will reach those points. However, the highway works against us if we want to reach a point anywhere left of the inflection point. If our target lies within this region, we will actually reach it faster as the highway flow becomes weaker.

3.1.3 2d Histogram of Reachability Fronts

When we looked at the relationship between reachability front and highway speed, every single reachability front was placed onto the same figure. The figures presented in Section 3.1.2 are misleading in that the reachability fronts appear to be uniformly distributed amongst the band. This may or may not be the case. The zero level sets may be more dense in some regions and more sparse in others.

We produce a 2d histogram of the reachability fronts in order to get a better sense of their distribution. We look at each grid cell in the domain and evaluate ϕ at each cell. We count the number of realizations for which $\phi = 0$ at that grid cell.

Because of the discretization of the spatial grid, few of the grid cells contain an actual level set. More often, the value of ϕ is a low, but finite value. We make the following assumption

$$\phi(i,j) \begin{cases} = 0, & \text{if } \phi(i,j) < t. \\ \neq 0, & \text{otherwise.} \end{cases} \tag{3.1}$$

$$t = a * \max(\phi) \tag{3.2}$$

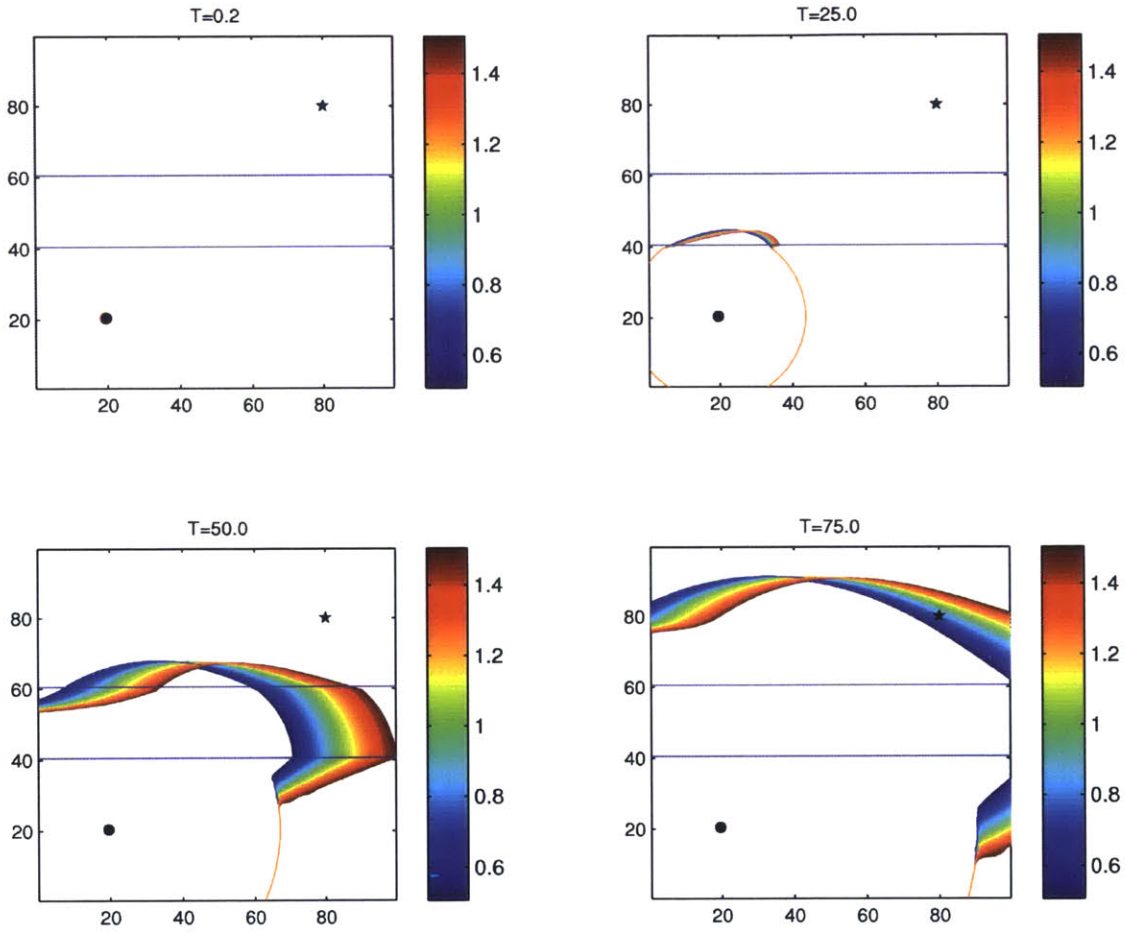

Figure 3-4: We plot the reachability fronts of every single realization. Each reachability front is colored according to its realization's highway strength (0.5 to 1.5 colorbar). Portions of the reachability front that have not yet entered the stochastic highway are unaffected. Portions that have seen uncertainty begin to develop a stochastic DO level-set band. The stochastic DO level-set band flips over on itself, splitting the domain into two regions. The highway flow helps us reach points in one region, and prevents us from reaching points in the other.

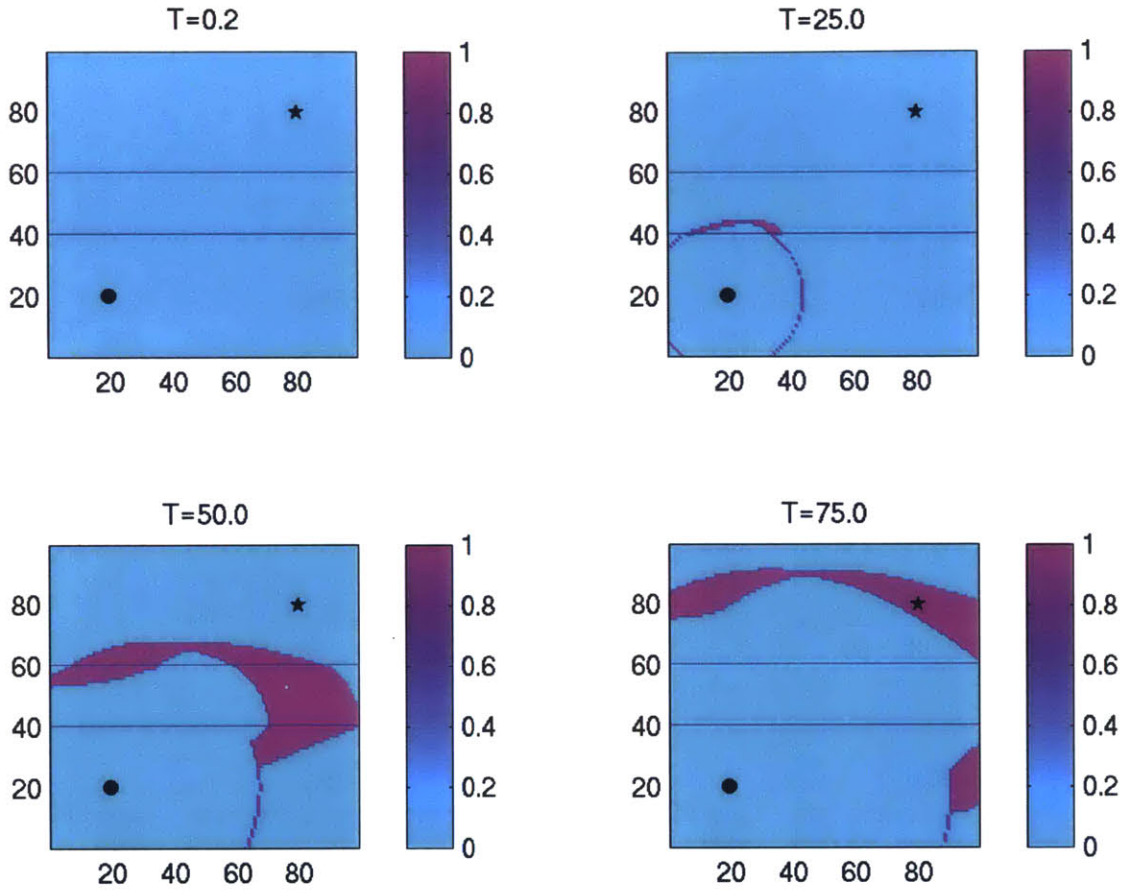

Figure 3-5: 2d histogram of the zero level sets of all realizations. The total number of DO realizations is 2,000. We truncate the color axis to verify that we have correctly counted the level sets.

In this case we choose $a = \frac{1}{1000}$. We can verify that our choice of a is correct by truncating the color axis to [0 1]. All grid cells with a value of zero will appear blue, and all grid cells with a finite value will appear purple. Figure 3-5 looks very similar to Figure 3-4. This confirms that we have correctly counted the zero level sets.

In Figure 3-6 we can see that the reachability fronts are definitely not uniformly distributed. The reachability fronts are most densely concentrated in regions where the stochastic DO level-set band is narrow. When the band becomes wider, the reachability fronts become sparser.

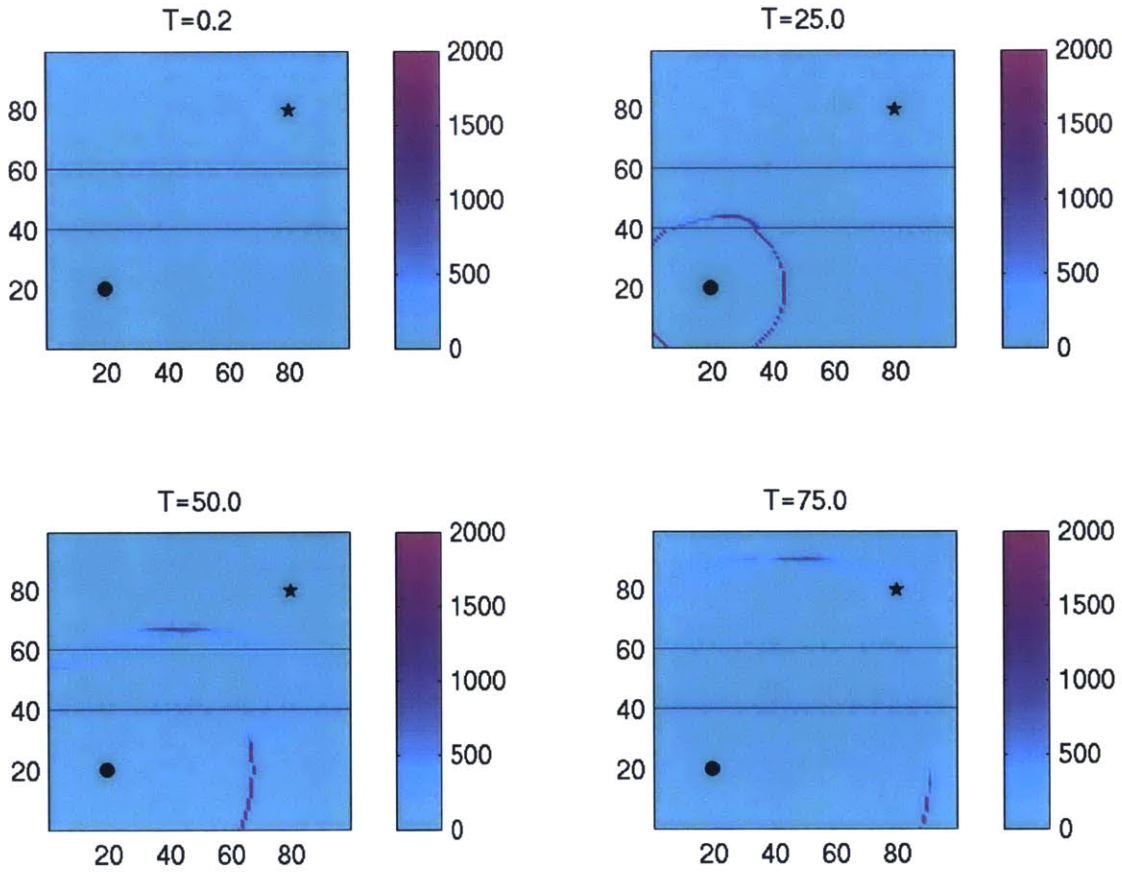

Figure 3-6: 2d histogram of the zero level sets of all realizations. The total number of DO realizations is 2,000. The reachability fronts are very dense when the stochastic DO level-set band is narrow, and become sparser when the stochastic DO level-set band widens.

Parameter	Value	Description
a	1	Size of domain in x-direction
b	1	Size of domain in y-direction
N_x	30	Number of cells in x-direction
N_y	30	Number of cells in y-direction
dx	0.0333	Spatial discretization in x-direction
dy	0.0333	Spatial discretization in y-direction
T	24	Total time of simulation in days
dt	.0058	Time Step in days
s	100	Number of DO modes
r	5	Number of flow field modes
m	5,000	Number of DO samples

Table 3.2: Parameters used for DO simulations of the double-gyre flow

3.2 Stochastic Double-Gyre Flow

The Double-Gyre (DG) flow is a more complex and realistic flow. The flow field is dynamic - it varies in both space and time. The double gyre flow is an idealized simulation of a wind-driven flow, similar to the Jet Stream in the Atlantic Ocean or the Kuroshio in the Pacific Ocean (for more see Dijkstra and Katsman, 1997, and Simmonet et al., 2009).

This wind-driven flow is modeled by the equations below:

$$\frac{\partial u}{\partial t} = -\frac{\partial p}{\partial x} + \frac{1}{Re}\Delta u - \frac{\partial (u^2)}{\partial x} - \frac{\partial (uv)}{\partial y} + fv + a\gamma_x \tag{3.3}$$

$$\frac{\partial v}{\partial t} = -\frac{\partial p}{\partial y} + \frac{1}{Re}\Delta v - \frac{\partial (v^2)}{\partial x} - \frac{\partial (vu)}{\partial y} + fu + a\gamma_y \tag{3.4}$$

$$0 = \frac{\partial x}{\partial y} + \frac{\partial v}{\partial y} \tag{3.5}$$

where Re is the Reynolds flow number, $f = \bar{f} + \beta y$ is the non-dimensional Coriolis coefficient, and $a = 10^3$ is the strength of the wind stress.

Snapshots of the double-gyre flow at various points during the simulations are shown in Figure 3-7.

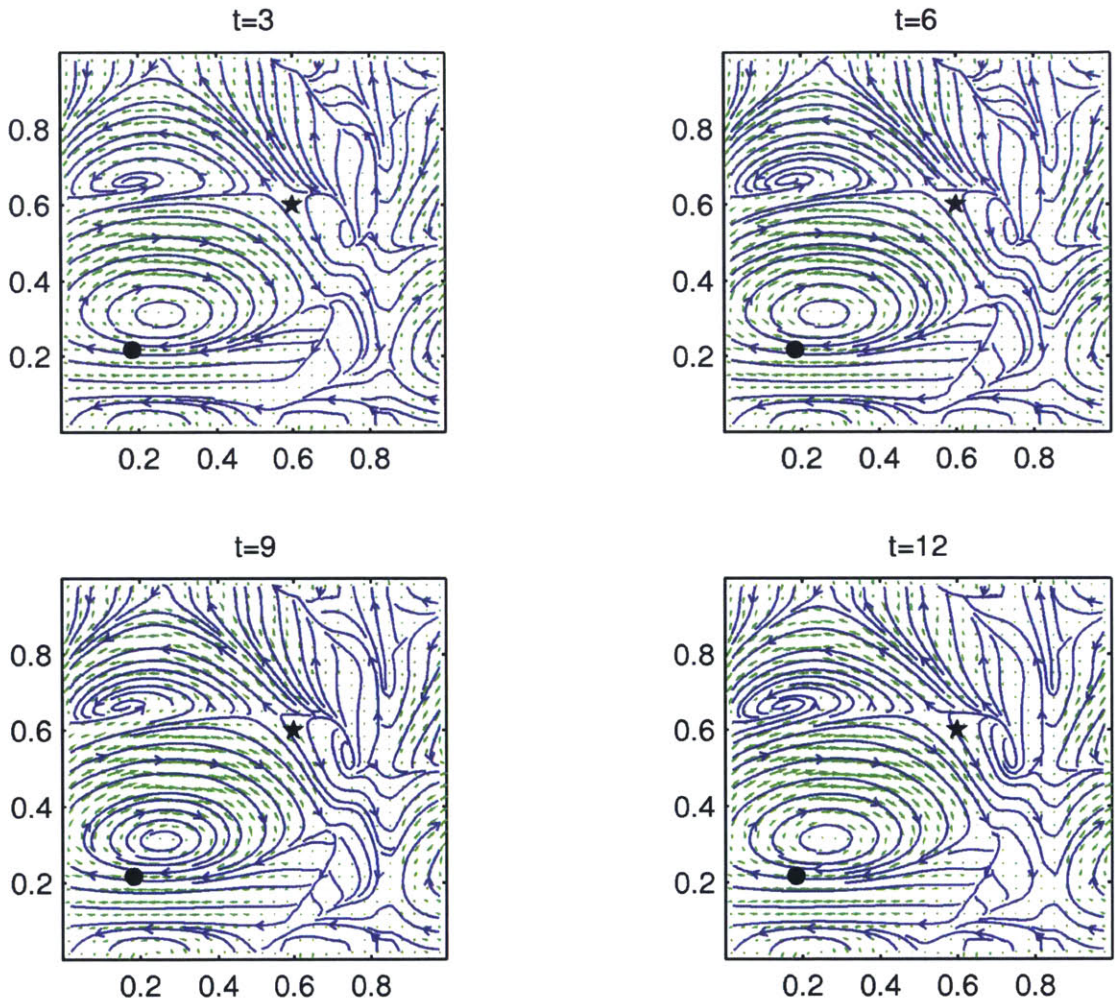

Figure 3-7: The wind-driven double gyre flow varies is dynamic, varying with time and space. The figure shows snapshots of the velocity flow field at various non-dimensional times during the simulation.

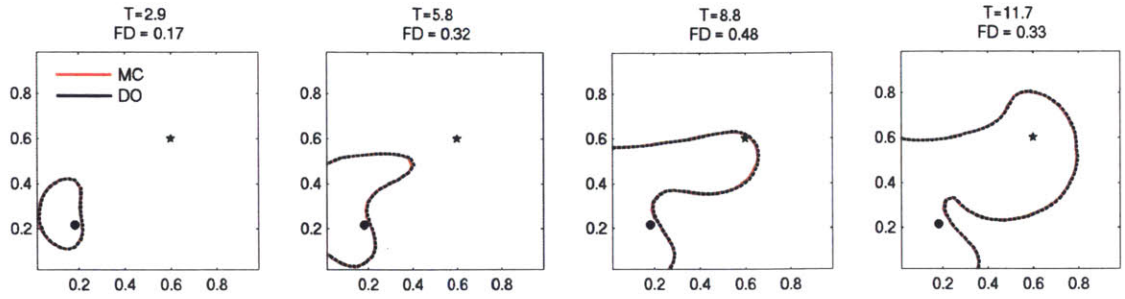

Figure 3-8: We compare a single realization's zero level set for the DO and MC simulations of the double gyre flow. The curves are nearly identical. Fréchet distance is normalized by grid cell size. The maximum Fréchet distance is less than the spacial resolution of the simulation.

3.2.1 Comparison of DO and MC level set

The stochastic double-gyre flow is substantially more complicated than the stochastic highway flow. Therefore, we did not run a full Monte Carlo simulation of the double-gyre flow.

For our purposes, verification of stochastic highway results is validate our faith in the new DO level set equations. However, as a sanity check, we run an MC simulation of the double-gyre flow with just one simulation.

We compare the reachability front of the DO and MC runs in Figure 3-8. We see that the curves are nearly identical. We also look at the discrete Fréchet distance between two curves, normalized by the size of the grid cells. The maximum Fréchet distance (FD $= 0.48$) is less than the spacial resolution of the DO simulation.

3.2.2 Reachability Front vs Time to Reach

In the stochastic double-gyre flow, velocity varies in both time and space. There is not a universal velocity that we can use to compare realizations, as there was with the stochastic highway. Instead, we look at the Time to Reach the target point.

The zero level set of every single level set curve is plotted onto Figure 3-9. Each curve is colored according to it's realizations Time to Reach. In this DO run, there are 5,000 realizations.

The stochastic double gyre flow is more complex than the stochastic highway. The

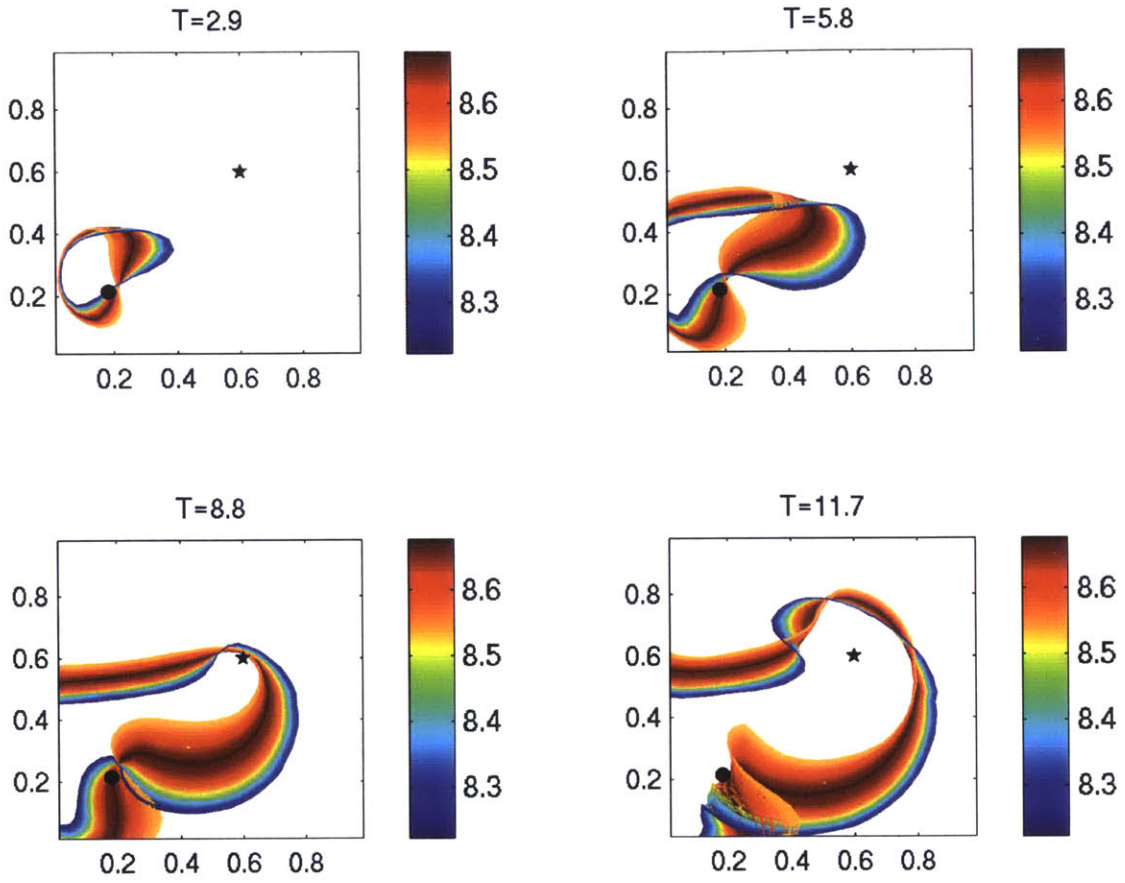

Figure 3-9: We plot the zero level sets of every single realization, colored by Time to Reach. Regions with a very wide stochastic DO level-set band indicate large amounts of uncertainty compared to regions with a narrow stochastic DO level-set band. The stochastic DO level-set band flips several times due to the complexity of the flow.

stochastic DO level-set band immediately develops and becomes quite wide in some regions. The stochastic DO level-set band flips over on itself multiple times.

3.2.3 2d histogram of Reachability Fronts

Once again we look at a 2d histogram of the reachability fronts. Figure 3-10 shows the histogram with a truncated color axis. It is very similar to Figure 3-9, confirming that we have correctly counted the zero level sets. The granularity in the histograms is due to the coarse grid: $N_x = 30$ for this DO run. Figure 3-11 shows that the distribution of the level sets is not uniform. In this DO run, there are 5,000 realizations.

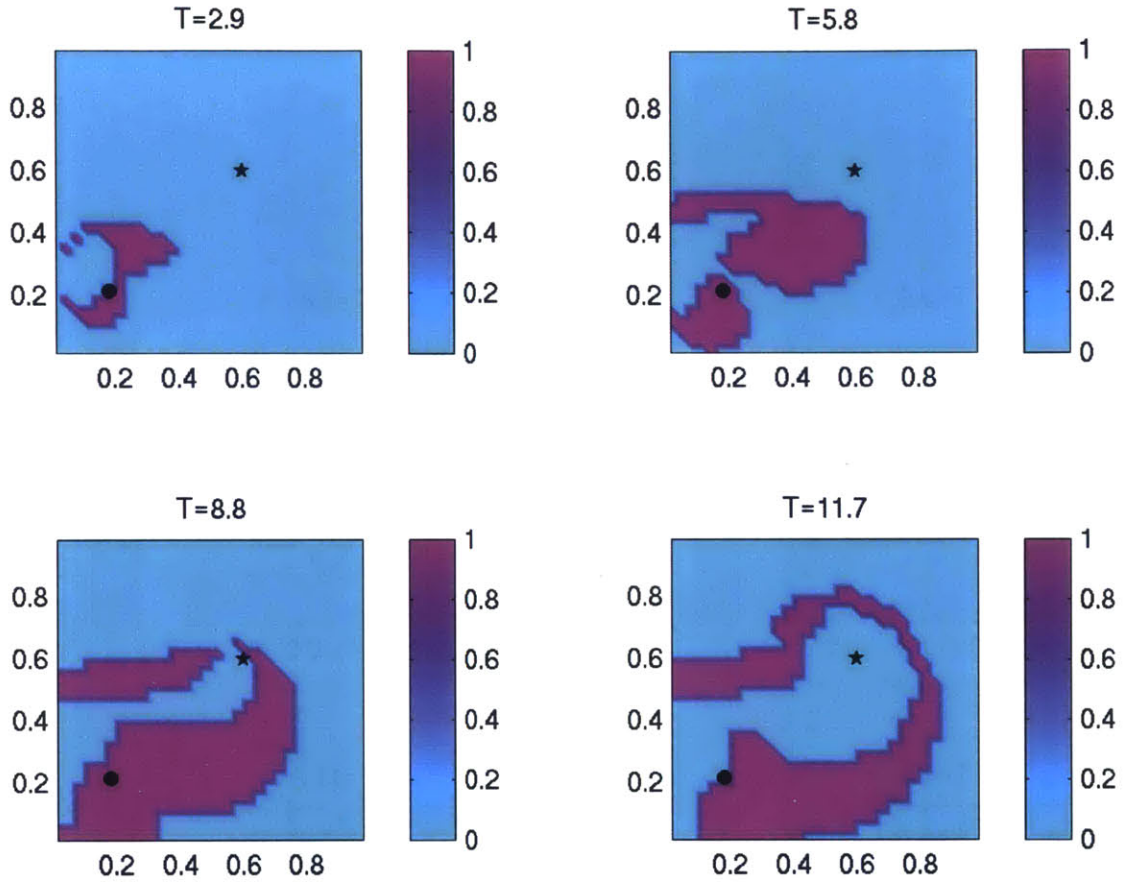

Figure 3-10: 2d histogram of the zero level sets with an alternate coloring scheme. The total number of DO realizations is still 5,000. We truncate the color axis to verify that we have correctly counted the zero level sets. All grid cells with a value of 0 appear blue. All grid cells with a finite value appear purple. This plot should look very similar to Figure 3-9.

In Figure 3-12, we present the same data but with an alternate color axis. The color axis is truncated to a maximum of 1,000 realizations. This allows us to better visualize the reachability fronts that occur with lower frequencies. The resulting image becomes more similar to a plot of all the reachability fronts. However, some regions are clearly very sparse in reachability fronts.

We confirm the uneven distribution by plotting 100 random zero level sets in Figure 3-13. Realizations are less likely to have zero level sets towards the middle of the stochastic DO level-set band. Zero level sets are found to be more likely to appear at the extremes of the band.

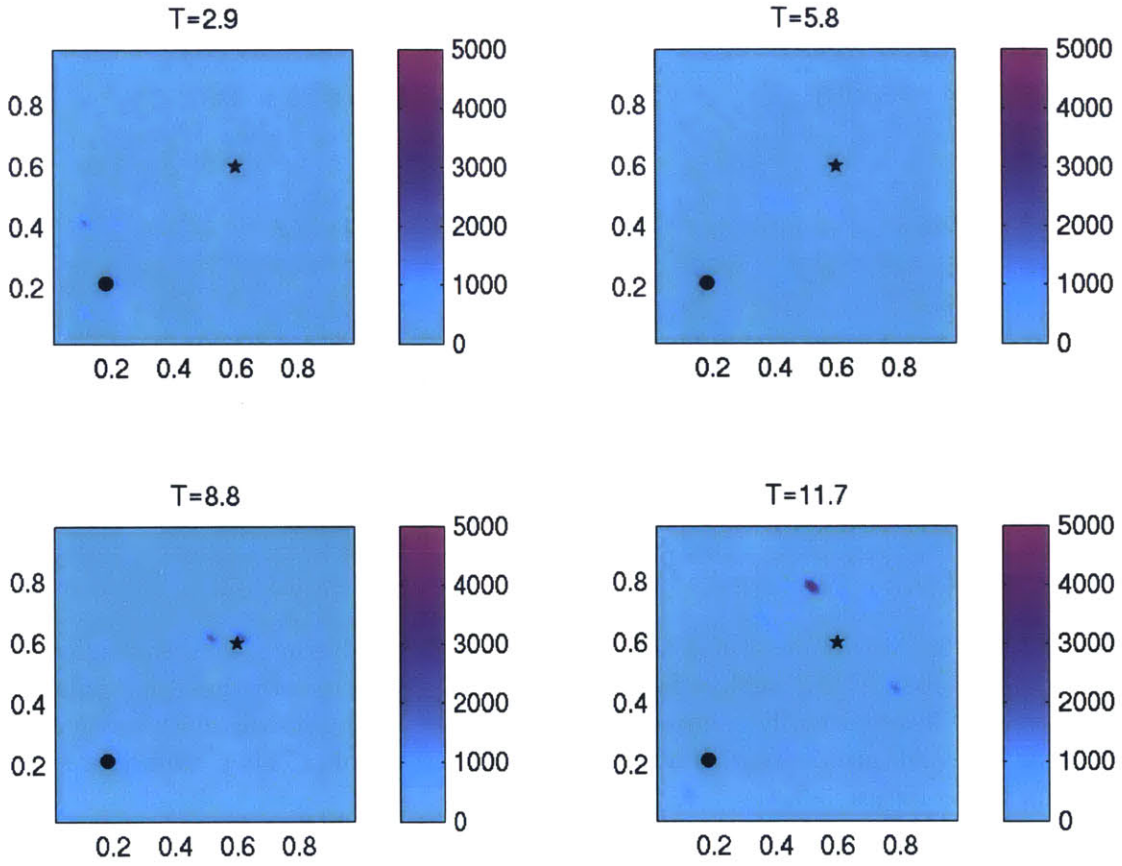

Figure 3-11: We create a 2d histogram of the zero level sets to visualize the probability distribution function. The total number of DO realizations is 5,000. The reachability fronts are not uniformly distributed. The faint outlines indicate that the fronts tend to gather at the extremes of the stochastic DO level-set band.

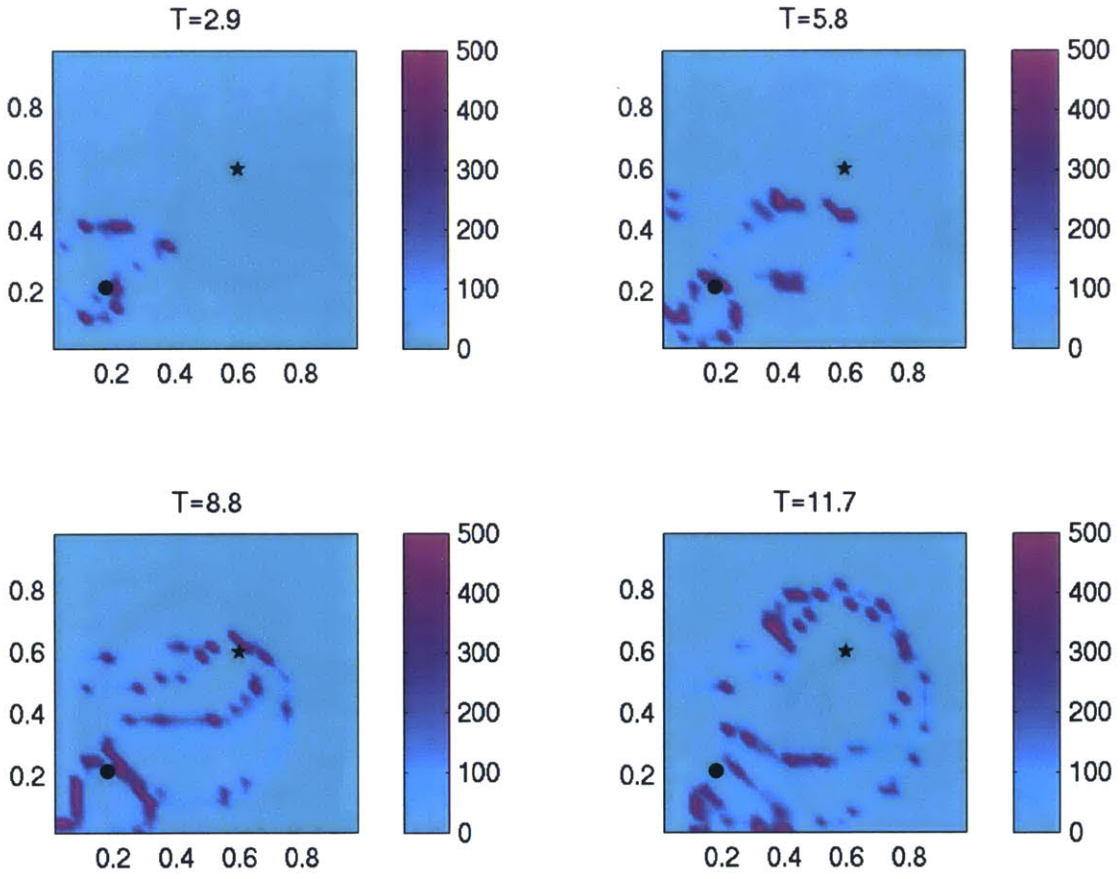

Figure 3-12: 2d histogram of the zero level sets with an alternate coloring scheme. The total number of DO realizations is still 5,000. The regions of blue that lie within the purple indicate regions within the stochastic DO level-set band that are very sparse.

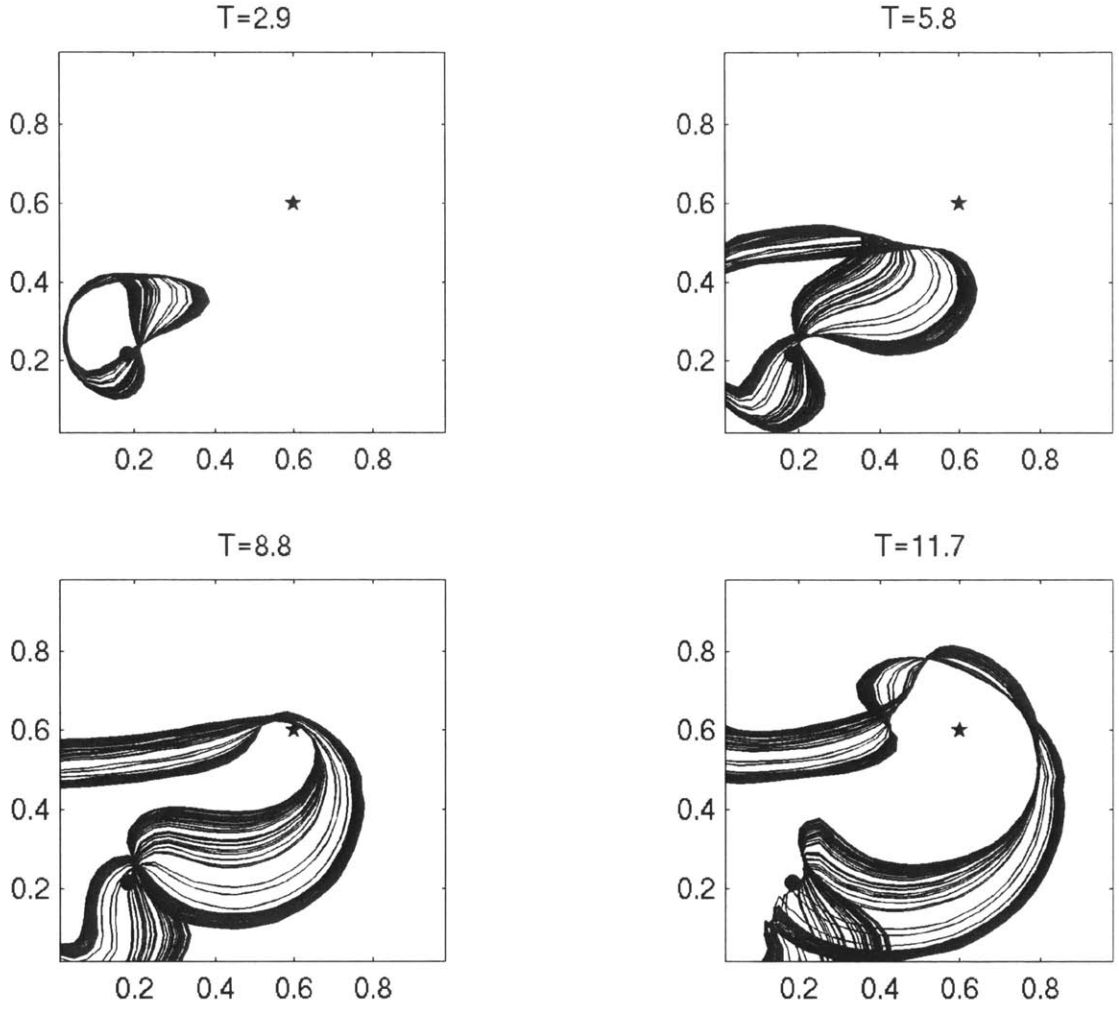

Figure 3-13: Plot of 100 random zero level sets. Realizations are less likely to have zero level sets towards the middle of the stochastic DO level-set band. Zero level sets are more likely to appear at the extremes of the band.

3.3 Conclusions

We used the stochastic highway flow to verify our new DO level set equations. A comparison of Times to Reach between a DO run and corresponding MC run confirms the DO results are correct. More than 97% percent of realizations had less than 0.5% error. The maximum Fréchet distance between DO and MC curves is less than the spacial resolution of the simulations.

We simulated a double-gyre flow with a DO run. We looked at reachability fronts for every realization compared to highway strength or Time to Reach. We observed the development of a stochastic DO level-set band once the reachability fronts see uncertainty in the flow. The stochastic DO level-set band was found to flip on itself, dividing the domain into separate regions of reachability. Certain regions of the domain are more reachable for some realizations, and the other regions are more reachable for other realizations. It may be useful to track the inflection points in the stochastic DO level-set bands. We may be able to map out distinct "regions of reachability" within the domain, in accord with the probability distribution function (PDF) of the flow field. We also note that the PDF of these currents is non-Gaussian and this affects the stochastic level-sets.

These plots are useful, but can also be misleading in that the reachability fronts appear to be uniformly distributed. The 2d histograms show that the reachability fronts are not uniformly distributed in our test cases. In the double-gyre flow, the reachability fronts tend to cluster towards the extremes of the stochastic DO level-set bands too. The middle of the bands tend to be sparse.

The 2d histogram is essentially a very simple estimate of the probability distribution function. The granularity in these plots are due to the spacial resolution of the grid. Further work may include the use of kernel dressing functions to obtain a more sophisticated estimate of the underlying PDF. Kernel dressing should also smooth out these plots.

Chapter 4

Future Work

4.1 KL and Taylor Gamma

The current implementation of the new stochastic DO level-set equations uses an MC approach to evaluating γ. We should be able to gain improved performance by deriving equations corresponding to a KL or Taylor realization of γ (Subramani, 2014 and Subramani et al., 2015). Existing energy-optimal path planning code can then be modified to implement the new KL or Taylor equations.

4.2 Further Analysis of Current Results

In uncertain flows, the stochastic DO level-set band may flip over on itself at certain points. These inflection points divide the domain into regions. Certain regions of the domain are more reachable for some realizations, and the other regions are more reachable for other realizations. It may be useful to track the inflection points in the level-set bands. We may be able to map out distinct "regions of reachability" within the domain, in accord with the uncertainty seen by the vehicles in the different regions.

The 2d histograms of the double-gyre flow show that the level sets tend to concentrate at the extremes of the stochastic DO level-set band, whereas the center of the band is quite sparse. Further work is required to understand why the level sets are distributed in this manner. Due to the DO methodology, the level sets evolve as

fast as possible. DO computation may be leading to the grouping of level sets at the extremes of the level-set band. It is also important to note that the coloring scheme depends on the chosen target point. All of this would need to be studied and further evaluated, also checking for implementation accuracy.

The 2d histogram is essentially a very simple estimate of the probability distribution function (PDF). The granularity in these plots are due to the spacial resolution of the grid. Further work may include the use of kernel dressing functions to obtain a more sophisticated estimate of the underlying PDF. Kernel dressing should also smooth out these plots.

4.3 Energy-Optimal Path Planning

The DO runs presented in this thesis have treated the vehicle speed as a constant variable. The equations and current code support the treatment of vehicle speed as a random variable. An obvious next step is to run DO simulations where both the flow field and vehicle speed are treated as stochastic variables. This would allow for energy-optimal path planning in uncertain flow fields. Analysis of such runs will be less straightforward. We anticipate further thought will be required to analyze and present the results of such runs in a meaningful and useful way.

Chapter 5

Conclusions

We have expanded on the path planning optimization work done by Lolla (2012)and Subramani et al. (2015). Specifically, we have extended the dynamically orthogonal level set equations used for energy-optimal path planning to account for uncertainties in the flow field. These equations were implemented by modifying the Energy-Optimal Path Planning Code to work with uncertain flow fields (Subramani, 2014).

The new DO equations have been verified against the results of an MC simulation for a simple canonical flow, the stochastic highway. The DO results are very close to the MC results, with more than 97% of realizations showing less than 0.5% error in Time to Reach. The maximum Fréchet distance between DO and MC curves was found to be less than the spacial resolution of the simulations.

We simulate a stochastic double-gyre flow. We explore two ways of visualizing the results from the new stochastic level set equations. We can plot all the reachability fronts, coloring each curve according to it's realizations highway speed or time to reach. We observe the development of a stochastic DO level-set band due to the uncertainty of the flow. The level-set band varies in width and flips over on itself at certain points. These inflection points divide the domain into regions of reachability. These plots can be misleading: the level sets appear to be uniformly distributed. 2d histograms of all the level sets show that they are not uniformly distributed.

We have only begun to explore the results of these new equations, and there is much more work that can be done. How exciting!

Bibliography

[1] Alt, H. and Godau, M., 1995 *Computing the fréchet distance between two polygonal curves.* International Journal of Computational Geometry & Applications, 5(01n02):75-91

[2] Dijkstra, H. and Katsman, C., 1997. *Temporal variability of the wind-driven quasi-geostrophic double gyre ocean circulation: Basic bifurcation diagrams.* Geophysics Astrophysics Fluid Dynamics, 85:195-232.

[3] Lermusiaux, P.F.J, 2007. *Adaptive Modeling, Adaptive Data Assimilation and Adaptive Sampling.* C.K.R.T. Jones and K. Ide, Eds. Physica D, Vol 230, 172-196.

[4] Lolla, T., P.F.J. Lermusiaux, M.P. Ueckermann and P.J. Haley, Jr., 2014. *Time-Optimal Path Planning in Dynamic Flows using Level Set Equations: Theory and Schemes.* Ocean Dynamics, 64, 10:1373-1397.

[5] Lolla, T.; Ueckermann, M.P.; Yigit, K.; Haley, P.J.; Lermusiaux, P.F.J., 2012. *Path planning in time dependent flow fields using level set methods,* 2012 IEEE International Conference on Robotics and Automation (ICRA), 166-173, 14-18 May 2012.

[6] Osher, S. and Sethian, J. A., 1988. *Fronts propagating with curvature-dependent speed: Algorithms based on Hamilton-Jacobi formulations.* Journal of Computational Physics, 79(1):12-49.

[7] Sapsis, T.P. and Lermusiaux, P.F.J., 2009. *Dynamically orthogonal field equations for continuous stochastic dynamical systems.* Physica D, 238, 2347-2360.

[8] Simmonet, E., Djikstra, H., and Ghil, M., 2009. *Bifurcation Analysis of Ocean, Atmosphere, and Climate Models.* Computational Methods for the Atmosphere and Oceans, volume XIV, p. 187-229.

[9] Subramani, D.N., 2014. *Energy Optimal Path Planning Using Stochastic Dynamically Orthogonal Level Set Equations.* SM Thesis, Massachusetts Institute of Technology, Computation for Design and Optimization Graduate Program, September 2014.

[10] Subramani, D.N., T. Lolla, P.J. Haley and P.F.J Lermusiaux, 2015. *A Stochastic Optimization Method for Energy-based Path Planning* Dynamic Data-driven Environmental Systems Science Conference (Eds. Ravela, Sandu et al), Springer Lecture Notes In Computer Science, In Press.

[11] Ueckermann, M.P., P.F.J. Lermusiaux and T.P. Sapsis, 2013. *Numerical Schemes for Dynamically Orthogonal Equations of Stochastic Fluid and Ocean Flows.* J. Comp. Phys., 233, 272-294.